NJC

PAPER

View Article Online
View Journal | View Issue

Cite this: *New J. Chem.*, 2019, **43**, 18277

Received 18th August 2019,
Accepted 16th October 2019

DOI: 10.1039/c9nj04273c

rsc.li/njc

Highly efficient CO_x-free hydrogen evolution activity on rod Fe_2N catalysts for ammonia decomposition†

Bowen Lei,[a] Jie Wen,*[a] Shan Ren,[b] Lianhong Zhang[a] and Hui Zhang*[a]

Ammonia decomposition is a critical method for CO_x-free hydrogen production, and many metal nitrides have been studied as excellent catalysts for NH_3 decomposition recently. Here, Fe_2N catalysts with rod, cubical and discoidal structures were prepared *via* nitrogenization of the corresponding morphologies of Fe_2O_3 precursors, which were obtained by a hydrothermal synthesis method. These Fe_2N catalysts were characterized by XRD, TEM, BET, XPS and Mössbauer spectroscopy, and the results showed that the morphologies of Fe_2O_3 precursors had a significant effect on the crystallite size and yield of the nitride phase of Fe_2N catalysts. The rod Fe_2N had a small crystallite size and a high relative nitrogen content among the three samples. The catalytic activity for hydrogen production *via* ammonia decomposition was measured using a micro-fixed bed reactor under conditions of conventional pressure and a GHSV of 6000 mL g_{cat}^{-1} h^{-1}. The rod Fe_2N exhibited a higher NH_3 conversion of 90% at 823 K compared with Fe_2N derived from cubical and discoidal Fe_2O_3, and maintained high stability for 40 h.

1. Introduction

The global community is being confronted with more and more complicated environmental pollution issues due to the large consumption of fossil fuels. It is urgent to search for renewable and clean energy sources to decrease the current level of dependence on fossil fuels. Recently, hydrogen production, which is recognized as one of the cleanest energy sources, has received great attention.[1–3] Considering the high hydrogen densities (17.6 wt%) and huge production of NH_3, the use of NH_3 to produce H_2 is a superior choice in comparison with currently used reforming processes of methane or methanol, which usually ends with potential CO_x release.[4] However, the rate of the NH_3 decomposition reaction is too slow to proceed, even at a very high temperature ($\sim$923 K). Hence, searching for suitable catalysts to promote NH_3 decomposition is extremely imperative. Though noble metal catalysts have exhibited satisfactory catalytic performance in NH_3 decomposition,[5–11] their high cost and scarcity strictly limited their extensive use in practical applications,[12–14] propelling us to find appropriate non-noble-metal candidates as NH_3 decomposition catalysts, such as transition metals Ni, Co, and Fe.[15–17]

To date, transition metal nitrides have drawn much attention in hydrodesulfurization (HDS), Fischer–Tropsch (F–T) processes, hydrodenitrogenation (HDN) and NH_3 decomposition.[18] Monometallic nitrides (VN_x, MoN_x and FeN_x)[19–23] and bimetallic nitrides (Ni–Mo–N and Co–Mo–N)[24–31] all have demonstrated excellent performance for NH_3 decomposition. Our previous reports have shown that Fe_2N played an active role in the enhanced catalytic ability of Fe_3O_4/CNTs in ammonia decomposition and the key was the effective control of the density of the Fe_2N active sites.[32] Recently, Leybo *et al.* have synthesized various Ni–Mo nitride catalysts derived from different precursors. These precursors had a significant effect on the composition and specific surface area of Ni–Mo nitride.[26]

The choice of the precursor greatly determined the physicochemical and catalytic properties of the final nitride product.[33,34] In this work, we obtained rod, cubical and discoidal structure Fe_2N nanocatalysts through nitrogenization of regular Fe_2O_3 with corresponding morphologies. The as-prepared nano-rod Fe_2N exhibited a higher NH_3 decomposition activity in comparison with both cubical and discoidal Fe_2N. The high catalytic activity of rod Fe_2N was due to its small crystallite size and relatively high nitrogen content.

2. Experimental methods

2.1 Chemical materials

Analytical grade aluminium subacetate ($Al(OH)C_4H_6O_4$) was purchased from Aldrich. Sodium hydroxide (NaOH), ferric

---

[a] *The Centre of New Energy Materials and Technology, College of Chemistry and Chemical Engineering, Southwest Petroleum University, Chengdu 610500, China. E-mail: huizhang@swpu.edu.cn, wenjie@swpu.edu.cn*

[b] *The Institute of Functional Nano & Soft Materials (FUNSOM), Jiangsu Key Laboratory for Carbon-Based Functional Materials & Devices, Soochow University, Suzhou 215123, China*

† Electronic supplementary information (ESI) available. See DOI: 10.1039/c9nj04273c

nitrate ($Fe(NO_3)_3 \cdot 9H_2O$), ammonium hydroxide solution (28%) and ethyl alcohol were all obtained from Chengdu Kelong Chemical Reagents Co., Ltd. All chemicals used in this work were not further purified. Deionized water was employed in all experiments.

2.2 Synthesis of catalysts

2.2.1 Synthesis of rod Fe_2N. In a typical synthesis procedure for a rod Fe_2O_3 precursor,[35] $Fe(NO_3)_3 \cdot 9H_2O$ (5 mmol) was dissolved in 20 mL deionized water (DI) to form a homogeneous solution and the pH was gradually adjusted to > 13 using 10 mL 3.0 M NaOH under stirring. The obtained solution was transferred to 50 mL Teflon-lined stainless-steel autoclaves and kept at 453 K for 6 h. Then the above product was separated *via* centrifugation and was washed several times with ethanol and water. The obtained solids were vacuum dried at 333 K for 12 h and then were calcined at 623 K for 4 h in air to obtain rod Fe_2O_3 (denoted as Fe_2O_3-R). Finally, the Fe_2O_3-R was heated to 773 K at a rate of 5 °C min^{-1} and kept at 773 K for 2 h in a 10 mL min^{-1} NH_3 flow to obtain rod Fe_2N (denoted as Fe_2N-R).

2.2.2 Synthesis of cubical Fe_2N. In a typical synthesis procedure for a cubical Fe_2O_3 precursor,[35] $Fe(NO_3)_3 \cdot 9H_2O$ (10 mmol) was dissolved in 20 mL DI and then 10 mL 0.6 M NaOH was gradually added to form a homogeneous solution under stirring, and the final pH of the solution was close to 2. The obtained solution was transferred to 50 mL Teflon-lined stainless-steel autoclaves and kept at 453 K for 12 h. Then the above product was separated *via* centrifugation and was washed several times with ethanol and water. The obtained solids were vacuum dried at 333 K for 12 h and then were calcined at 623 K for 4 h in air to obtain cubical Fe_2O_3 (denoted as Fe_2O_3-C). Finally, the Fe_2O_3-C was heated to 773 K at a rate of 5 °C min^{-1} and kept at 773 K for 2 h in a 10 mL min^{-1} NH_3 flow to obtain cubical Fe_2N (denoted as Fe_2N-C).

2.2.3 Synthesis of discoidal Fe_2N. In a typical synthesis procedure for a discoidal Fe_2O_3 precursor,[36] $Fe(NO_3)_3 \cdot 9H_2O$ (2 mmol) was dissolved in 10 mL DI to form a homogeneous solution, and the required 20 mL of 0.05 M $Al(OH)C_4H_6O_4$ was added dropwise under stirring. After this, 10 mL ammonium hydroxide solution was added dropwise. The obtained solution was transferred to 50 mL Teflon-lined stainless-steel autoclaves and kept at 433 K for 16 h. Then the above product was separated *via* centrifugation and was washed several times with ethanol and water. The obtained solids were vacuum dried at 333 K for 12 h and then were calcined at 623 K for 4 h in air to obtain discoidal Fe_2O_3 (denoted as Fe_2O_3-D). Finally, the Fe_2O_3-D was heated to 773 K at a rate of 5 °C min^{-1} and kept at 773 K for 2 h in a 10 mL min^{-1} NH_3 flow to obtain discoidal Fe_2N (denoted as Fe_2N-D).

2.3 Characterization

The crystallite structure was analyzed by Powder X-ray diffraction (XRD, Rigaku MiniFlex-600) using a copper target as the radiation source (λ = 0.15406 nm). A transmission electron microscope (TEM, Hitachi-7700) was used to characterize the morphologies of the samples operating at 100 kV. The high resolution transmission electronic microscopy (HRTEM) image and energy dispersive X-ray spectroscopy (EDS) mapping images were obtained using a JEM-2100F with a spherical aberration corrector operating at 200 kV. N_2 adsorption/desorption isotherms of the samples were obtained using a Micromeritics 2020 at 77 K. The specific surface area was calculated using a multipoint Brunauer–Emmett–Teller (BET) method. The total pore volume was estimated from the N_2 adsorption capacity at P/P_0 = 0.995. The Barrett–Joyner–Halenda (BJH) method was used to measure the average pore size. X-ray photoelectron spectroscopy (XPS) was performed using a PHI5000 Verasa and an aluminum target as the excitation source. A constant acceleration spectrometer with the Co γ-quantum source in the Rh matrix was used to collect the Fe Mössbauer spectrum at room temperature. The spectra were fitted by the least squares fitting procedure through the Lorentzian curve. All the isomer shifts (IS) were referenced to the room temperature α-Fe centroid.

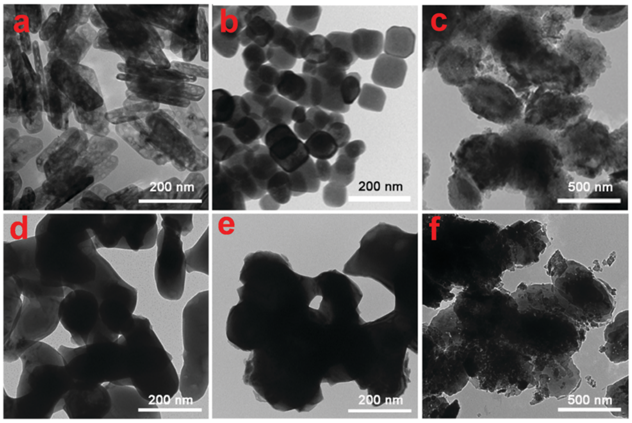

Fig. 1 TEM images of (a) Fe_2O_3-R, (b) Fe_2O_3-C, (c) Fe_2O_3-D, (d) Fe_2N-R, (e) Fe_2N-C and (f) Fe_2N-D.

2.4 Catalytic performance measurement

The activity measurement of catalysts for ammonia decomposition was carried out using a micro-fixed bed reactor of quartz glass (inner diameter = 4 mm). Typically, 100 mg of catalysts was charged into the reactor and pure ammonia gas (99.999% NH_3, Jinkexing Gas Co., Ltd) was passed into the reactor with 6000 mL g_{cat}^{-1} h^{-1} gas hourly space velocity (GHSV). The temperature was gradually increased at a rate of 5 K min^{-1} and kept for 30 min at each reaction temperature. The reaction products were analyzed using a gas chromatograph (SC-200) with a Porapak Q column and a thermal conductivity detector with Ar as the carrier gas. The ammonia conversion was calculated using eqn (1):

$$X_{NH_3} = \frac{(A_{NH_3,in} - A_{NH_3,out})}{A_{NH_3,in}} \times 100\% \quad (1)$$

where $A_{NH_3,in}$ is the total concentration of ammonia in feed gas, and $A_{NH_3,out}$ is the unconverted concentration of ammonia.

3. Results and discussion

3.1 Characterization of catalysts

The TEM images of the synthesized Fe_2O_3 samples are shown in Fig. 1. Fig. 1a shows that uniform Fe_2O_3-R with a rod structure was obtained. The average length of Fe_2O_3-R was 227 nm as seen from Fig. S1a (ESI†). The Fe_2O_3-R showed large numbers of pores, which was attributed to the dehydration effect during calcination.[35] Fig. 1b and c show that cubical and discoidal Fe_2O_3 were obtained with slight modifications in the experimental procedure. Fig. S1b and c (ESI†) show that the average sizes of Fe_2O_3-C and Fe_2O_3-D were 83 nm and 450 nm, respectively. And then the three Fe_2O_3 precursors were heated at 773 K under a NH_3 flow for 2 h and Fe_2N species were formed. This conversion of Fe_2O_3 to Fe_2N was believed to be depicted using eqn (2).[37]

$$2Fe_2O_3 + 4NH_3 \rightarrow 2Fe_2N + 6H_2O + N_2 \qquad (2)$$

The TEM images of the Fe_2N samples are shown in Fig. 1d–f. They indicated that the corresponding Fe_2O_3 morphologies were well maintained after the conversion, although a slight agglomeration of Fe_2N particles was observed.

The XRD patterns of Fe_2O_3 with rod, cubic and discoidal shapes are shown in Fig. 2a. They indicated that the diffraction peaks of the three samples were basically the same and corresponded to the hexagonal phase Fe_2O_3 (PDF No. 02-0919). The XRD patterns of Fe_2N with different shapes are displayed in Fig. 2b. They clearly indicated that the diffraction peaks at 2θ of 37.6°, 40.8°, 43.0°, 56.8°, 67.9° and 76.1° were attributed to the (100), (002), (101), (102), (110) and (103) facets of the hexagonal phase Fe_2N (PDF No. 02-1206). Additionally, the diffraction peak at 2θ of 36.1° corresponded to the (311) facet of Fe_3O_4 (PDF No. 75-0449) in Fe_2N-D. The crystallite sizes of the Fe_2N samples were calculated using Scherrer's equation and the results are listed in Table 1. The crystallite sizes of Fe_2N-R and Fe_2N-D were 50.8 nm and 41.3 nm, respectively. It can be noted that the crystallite size of Fe_2N-C was much larger than those of Fe_2N-R and Fe_2N-D. The results indicated that the crystallite size of the Fe_2N-C was the largest, and the crystallite sizes of Fe_2N-R and Fe_2N-D were similar in the three samples.

Table 1 The calculation results by Scherrer's equation

Samples	$2\theta/°$	*Hkl*	FWHM/rad	D/nm
Fe_2N-R	42.9	101	0.195	50.8
Fe_2N-C	42.9	101	0.127	>100.0
Fe_2N-D	43.2	101	0.230	41.3

Table 2 Structural properties of Fe_2N with different morphologies

Samples	Specific surface area ($m^2\ g^{-1}$)	Pore volume ($cm^3\ g^{-1}$)	Average pore size (nm)
Fe_2N-R	7.25	0.010	14.8
Fe_2N-C	2.13	0.005	26.3
Fe_2N-D	21.96	0.080	18.2

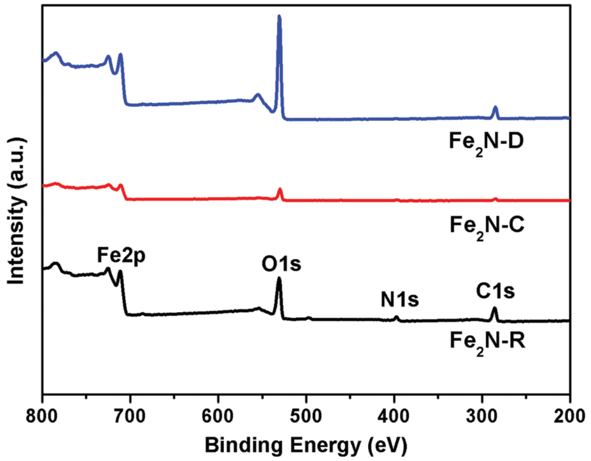

Fig. 3 X-ray photoelectron survey spectra of Fe_2N with different morphologies.

The BET specific surface area, pore volume and average pore size of as-prepared Fe_2N with different morphologies were obtained from N_2 adsorption–desorption isotherms at 77 K. The results are listed in Table 2. The average pore sizes of Fe_2N were in the range of 15 to 26 nm. The pores should be ascribed to the voids originating from the porous Fe_2O_3. Fig. S2 (ESI†) shows that the Fe_2O_3 samples adsorbed/desorbed N_2 gas at 77 K

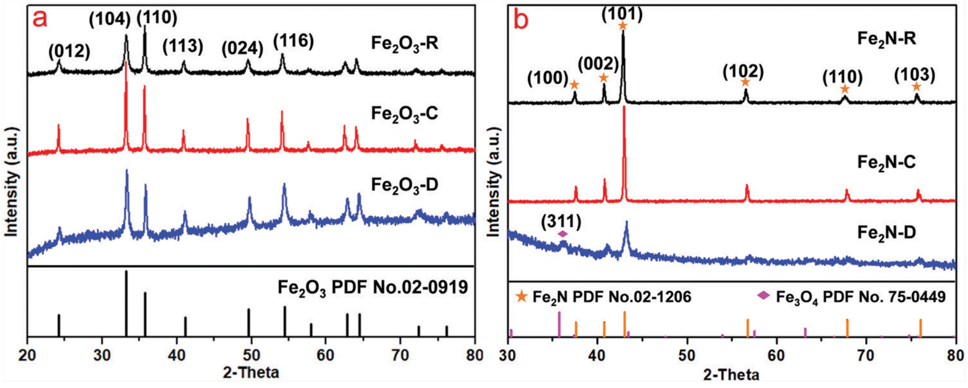

Fig. 2 XRD patterns of (a) Fe_2O_3 and (b) Fe_2N with different morphologies.

displaying IV isotherms were characterized as mesoporous materials, according to the IUPAC definition. Moreover, the specific surface areas of the Fe_2N samples were in the order of Fe_2N-D > Fe_2N-R > Fe_2N-C, which was the same as that of Fe_2O_3 samples (Table S1, ESI†). However, the Fe_2N samples exhibited lower specific surface areas compared with Fe_2O_3 samples, which could be attributed to the slight agglomeration of particles after nitrogenization, as can be seen from the TEM results.

To further characterize the electronic structure and elemental composition of Fe_2N with different morphologies, XPS analysis was carried out. As shown in Fig. 3, the wide-scan XPS spectrum of Fe_2N showed four strong peaks at binding energies (BE) of

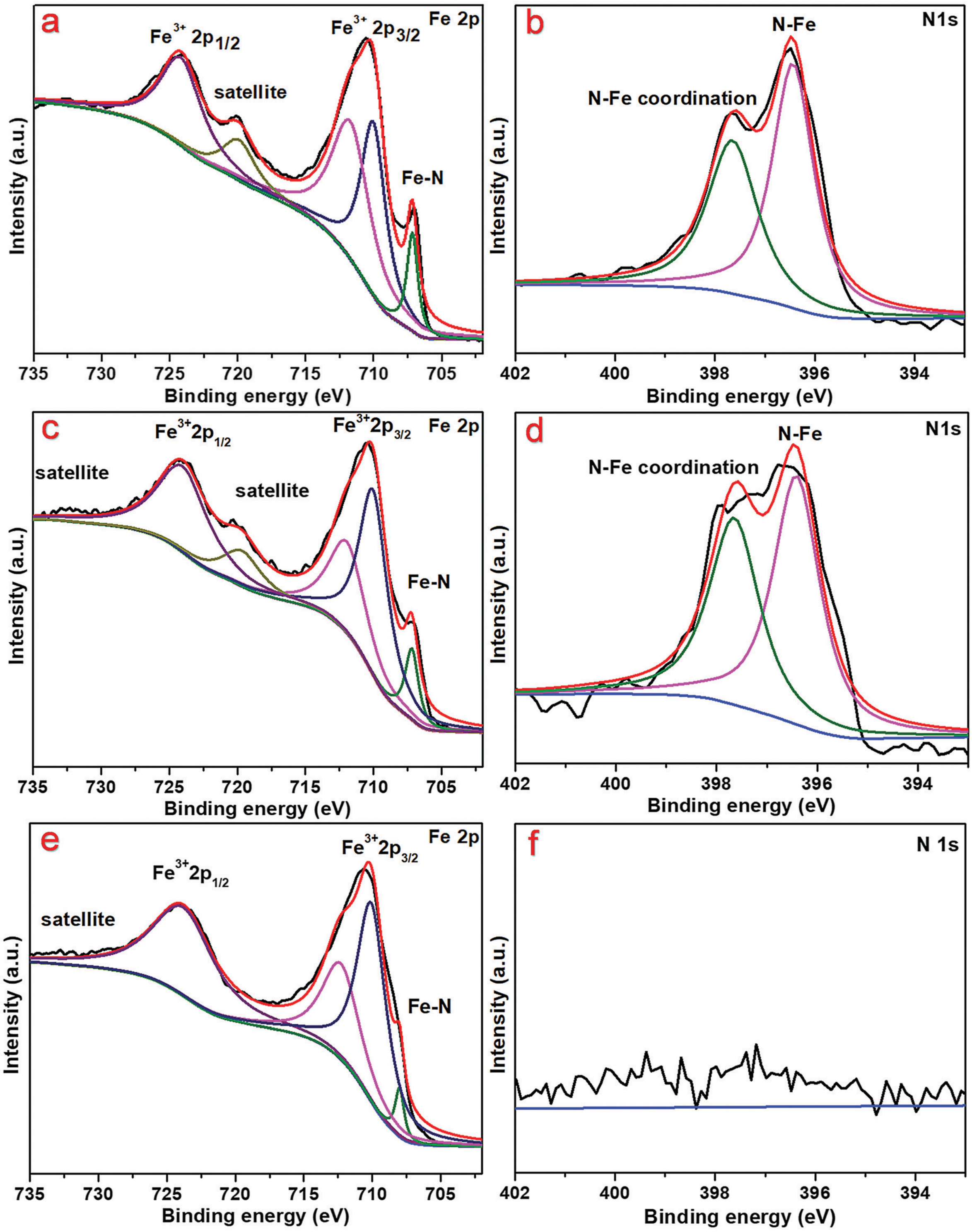

Fig. 4 High resolution XPS spectra of Fe 2p and N 1s of (a and b) Fe_2N-R, (c and d) Fe_2N-C, (e and f) Fe_2N-D.

Table 3 XPS analysis of the Fe, N, C and O contents and the N/Fe atom ratio

	Element contents (at%)				
Samples	Fe	N	C	O	N/Fe atom ratio (%)
Fe_2N-R	18.93	5.97	33.75	41.35	31.54
Fe_2N-C	28.16	7.47	24.24	40.13	26.53
Fe_2N-D	15.64	1.07	20.16	63.14	6.84

284.8 eV, 397.5 eV, 530.5 eV and 710.5 eV corresponding to C 1s, N 1s, O 1s and Fe 2p, respectively. The C 1s peak at 284.8 eV was the internal standard. The high resolution Fe 2p spectra of Fe_2N-R, Fe_2N-C and Fe_2N-D are shown in Fig. 4a, c and e, respectively. They all showed two strong peaks at BEs of 710.5 eV and 724.2 eV corresponding to Fe $2p_{3/2}$ and Fe $2p_{1/2}$, which were attributed to FeO_x species.[38] These FeO_x were formed by the surface oxidation of Fe_2N and it did not change the relative nitrogen content of Fe_2N, which has been reported by others.[32,39] In addition, the peak at 707.2 eV should be attributed to Fe–N.[32] The high resolution N 1s spectra of Fe_2N-R, Fe_2N-C and Fe_2N-D are shown in Fig. 4b, d and f, respectively. The XPS peaks of 396.4 and 397.7 eV can be assigned to N–Fe and N–Fe coordination compounds, respectively.[32,40] Since the peak intensity of N 1s of Fe_2N-D was too weak, and the error of the peak fitting was big, so the peak fitting was ignored. The XPS analysis data of element contents are listed in Table 3, indicating that the N/Fe atom ratio of the three Fe_2N catalysts was in the order of Fe_2N-R > Fe_2N-C > Fe_2N-D. The relative nitrogen content of Fe_2N-R was the highest among the three samples.

To further explore the structure of Fe_2N-R, we performed HRTEM imaging and EDS mapping at the edge of Fe_2N-R as shown in Fig. 5a and b. Fig. 5a shows a clear boundary between the Fe_2N nanocrystal and a surface FeO_x coating.[40] The surface oxidation phenomena have also been reported for MoP and MoN.[41] This was also consistent in the presence of the O element on the surface from the XPS study. However, FeO_x could not be detected by XRD, proving that FeO_x were amorphous species, or that the quantity of FeO_x was too small to be picked up by XRD, or that oxygen existed in the form of iron oxynitride. Furthermore, Fig. 5b clearly shows the homogeneous distribution of both Fe and N elements within the particles.

To further explore the composition of Fe_2N-R, Fe Mössbauer spectroscopy measurements were carried out as shown in Fig. 6 and Table 4. The results indicated that ζ-Fe_2N, ε-Fe_xN ($x \leq 2.1$) and O_x–Fe^{III}–N_4 species accounted for 49.14%, 42.3% and 8.6% in Fe_2N-R, respectively. This meant the main species were ζ-Fe_2N and ε-Fe_xN in Fe_2N-R. Also, a small amount of O_x–Fe^{III}–N_4 species were formed due to the surface oxidation of Fe_2N, which was consistent with the HRTEM and XPS results.[39,41]

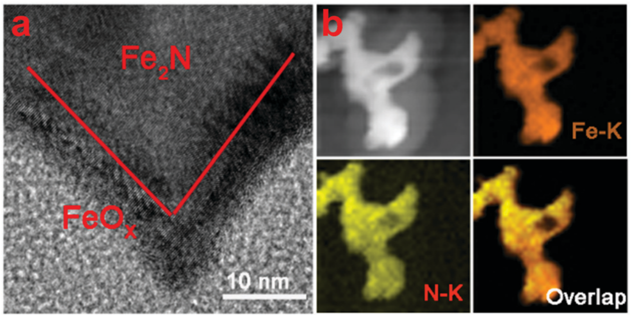

Fig. 5 (a) HRTEM image and (b) EDS mapping of Fe_2N-R.

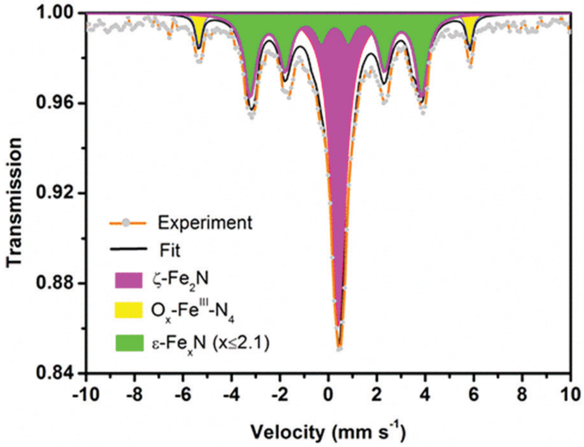

Fig. 6 Fe Mössbauer spectra of the Fe_2N-R catalyst at room temperature.

3.2 Catalytic activity testing

The NH_3 decomposition reaction test was carried out at a gas hourly space velocity (GHSV) of 6000 mL g_{cat}^{-1} h^{-1}. As shown in Fig. 7a, the activity of Fe_2N-R was superior to that of Fe_2N-C and Fe_2N-D under the same condition. Specifically, the NH_3 conversion of Fe_2N-R was 30% at 723 K, largely exceeding the conversion delivered by both Fe_2N-C and Fe_2N-D at 723 K. Similarly, Fe_2N-R exhibited 68% conversion at 773 K, whereas the NH_3 conversion of Fe_2N-C and Fe_2N-D was lower than 50%. Fig. 7b shows the Arrhenius fitting curves over three Fe_2N catalysts with different morphologies. The activation energies of Fe_2N-R, Fe_2N-C, and Fe_2N-D were 128.21 kJ mol^{-1}, 149.50 kJ mol^{-1} and 138.93 kJ mol^{-1}, respectively. Among these Fe_2N catalysts, Fe_2N-R has the lowest activation energy, which is well correlated with the highest catalytic activity of Fe_2N-R.

Our previous work has reported that Fe_2N was the main active component for the ammonia decomposition reaction.[32] The XPS results showed that Fe_2N-R had a higher N/Fe atom ratio than Fe_2N-C and Fe_2N-D, indicating that more Fe_2N species were formed on Fe_2N-R than on the other two catalysts. Also, small crystallite size Fe_2N-R was observed from the XRD pattern. Therefore, the Fe_2N-R had the optimal catalytic activity for ammonia decomposition among the three catalysts due to the high content and good dispersion of Fe_2N species. Although Fe_2N-C had more Fe_2N content than Fe_2N-D, they exhibited a similar catalytic activity because of the big crystallite size of Fe_2N-C (Table 1). These results indicated that the morphologies of the Fe_2O_3 precursor had a great influence on the elemental composition and crystallite size of the final product, which in turn affected the final catalytic activity. The Mössbauer measurements showed that the main species were ζ-Fe_2N and ε-Fe_xN ($x \leq 2.1$) in Fe_2N-R. It has been reported in the literature

Table 4 Fe Mössbauer parameters of the Fe_2N-R catalyst at room temperature

Catalysts		CS (mm s^{-1})	QS (mm s^{-1})	H (kOe)	A (%)	Assignment
Fe_2N-R	Singlet	0.4169(56)	—	—	49.1(90)	ζ-Fe_2N
	Sextet 1	0.2260(20)	0.0160(20)	346.40(14)	8.6(14)	O_x–Fe^{III}–N_4
	Sextet 2	0.2850(13)	0.0230(12)	219.23(89)	42.3(18)	ε-Fe_xN ($x \leq 2.1$)

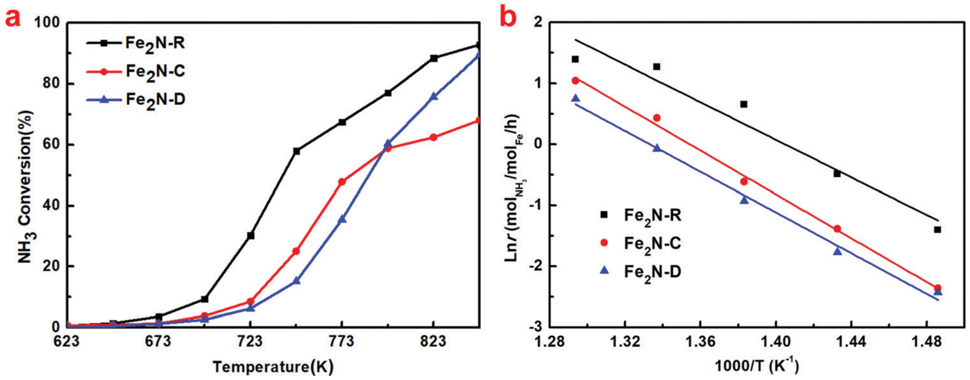

Fig. 7 (a) NH_3 decomposition reaction test over Fe_2N-R, Fe_2N-C, and Fe_2N-D. (b) Arrhenius plots over Fe_2N-R, Fe_2N-C, and Fe_2N-D from 673 K to 773 K. The reaction condition: 100 mg catalyst, 0.1 MPa and 6000 mL g_{cat}^{-1} h^{-1}.

that both species exhibited an excellent catalytic activity for ammonia decomposition.[32,42] This was why Fe_2N-R has a high activity for ammonia decomposition.

A comparison of the catalytic activities of different Fe based catalysts for ammonia decomposition are shown in Table 5.[31,43–46] This indicated that the Fe_2N-R catalyst exhibited excellent catalytic activity. The ammonia decomposition reaction test at a high GHSV of 24 000 mL g_{cat}^{-1} h^{-1} has been carried out as shown in Fig. S3a (ESI†). With the increase of GHSV from 6000 mL g_{cat}^{-1} h^{-1} to 24 000 mL g_{cat}^{-1} h^{-1}, the NH_3 conversion decreased at the same temperature. This indicated that the relatively low GHSV condition benefited the ammonia decomposition reaction, which was consistent with the report in the literature.[7] However, the Fe_2N-R also maintained 90% NH_3 conversion at 873 K with a high GHSV of 24 000 mL g_{cat}^{-1} h^{-1} as listed in Table 5.

The NH_3 decomposition stability of the Fe_2N-R catalyst was obtained by a 40 h reaction test at 6000 mL g_{cat}^{-1} h^{-1} as shown in Fig. 8. It could be clearly seen that the catalytic activity was almost unchanged in the 40 h test. The stability test of ammonia decomposition at a high GHSV of 24 000 mL g_{cat}^{-1} h^{-1} has also been carried out as shown in Fig. S3b (ESI†). When GHSV was increased from 6000 mL g_{cat}^{-1} h^{-1} to 24 000 mL g_{cat}^{-1} h^{-1}, the NH_3 conversion decreased at the same temperature, but the catalytic activity remained stable after 36 hours for ammonia decomposition.

Table 5 Comparison of the catalytic activity of different catalysts for ammonia decomposition based on the reported data

Catalysts	Temperature (K)	GHSV (mL g_{cat}^{-1} h^{-1})	NH_3 conversion (%)	Ref.
Fe_2N-R	823	6000	90	Present
Fe_2N-R	848	6000	93	Present
Fe_2N-R	873	24 000	90	Present
Fe_3Mo_3N	823	6000	78	31
Fe/CNTs	973	5000	75	43
Fe/CNFs	873	6500	51	44
Fe_2O_3/CMK-5	873	7500	92	45
Fe_3O_4@CeO_2	873	24 000	80	46
Fe_3O_4@TiO_2	873	24 000	89	46

Fe_2N-R after NH_3 decomposition reaction at different temperatures was denoted as used Fe_2N-R. The TEM image of the used Fe_2N-R is displayed in Fig. 9a. It can be seen that, compared with the fresh Fe_2N-R, the morphology of the used Fe_2N-R did not change significantly. The XRD pattern of the used Fe_2N-R is displayed in Fig. 9b, indicating that the main phase was still Fe_2N and its crystallite size (57.2 nm, in the inset) had little change compared with fresh Fe_2N-R (50.8 nm). Fig. 9c shows the XRD pattern of Fe_2N-R after the stability test. It could be observed that no new peaks appeared and its

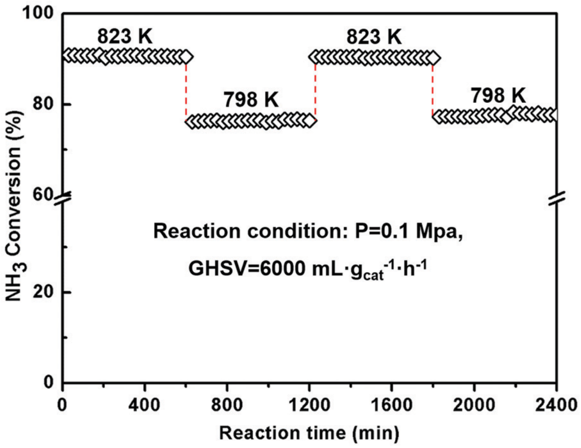

Fig. 8 NH_3 decomposition stability test of Fe_2N-R (GHSV = 6000 mL g_{cat}^{-1} h^{-1}).

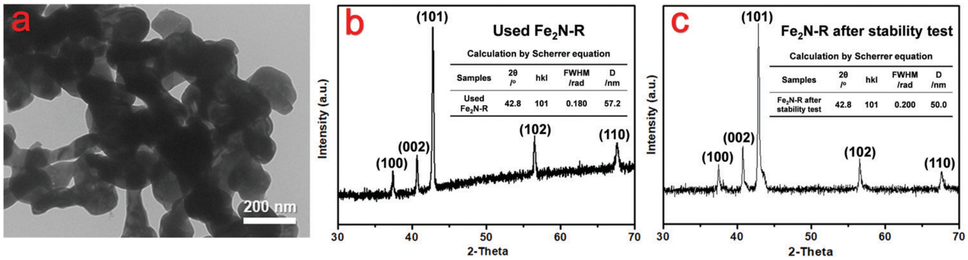

Calculation by Scherrer equation

Samples	2θ /°	hkl	FWHM /rad	D /nm
Used Fe_2N-R	42.8	101	0.180	57.2

Calculation by Scherrer equation

Samples	2θ /°	hkl	FWHM /rad	D /nm
Fe_2N-R after stability test	42.8	101	0.200	50.0

Fig. 9 (a) TEM image and (b) XRD pattern of the used Fe_2N-R, and (c) XRD pattern of Fe_2N-R after stability test.

crystallite size was 50.0 nm (in the inset), which was almost the same as the fresh Fe_2N-R. These results confirmed the high stability of the phase structure of Fe_2N-R. This was responsible for the high catalytic stability of Fe_2N-R.

4. Conclusion

It was found that the shapes of Fe_2O_3 precursors had an important influence on the crystallite size, active component content and catalytic performance of the corresponding Fe_2N catalysts for NH_3 decomposition. The prepared Fe_2N-R exhibited a small crystallite size as well as a high relative nitrogen content, resulting in the best catalytic activity compared with both Fe_2N-C and Fe_2N-D for NH_3 decomposition. These results demonstrated that our strategy would have a promising application in the design of more active catalysts for various industrial applications.

Conflicts of interest

There are no conflicts to declare.

Acknowledgements

This work was supported by the National Natural Science Foundation of China (21406184).

References

1 J. A. Turner, *Science*, 2004, **5686**, 972–974.
2 G. W. Crabtree, M. S. Dresselhaus and M. V. Buchanan, *Phys. Today*, 2004, **34**, 7.
3 H. Zhang, M. L. Huang, J. Wen, Y. P. Li, A. R. Li, L. H. Zhang, A. M. Ali and Y. D. Li, *Chem. Commun.*, 2019, **55**, 4699–4702.
4 S. Yin, Q. Zhang, B. Xu, W. Zhu, C. Ng and C. Au, *J. Catal.*, 2004, **224**, 384–396.
5 Y. F. Chang, J. G. McCarty, E. D. Wachsman and V. L. Wong, *Appl. Catal., B*, 1994, **4**, 283–299.
6 S. Ren, F. Huang, J. Zheng, S. Chen and H. Zhang, *Int. J. Hydrogen Energy*, 2017, **42**, 5105–5113.
7 X. Ju, L. Liu, P. Yu, J. Guo, X. Zhang, T. He, G. Wu and P. Chen, *Appl. Catal., B*, 2017, **211**, 167–175.
8 T. Furusawa, M. Shirasu, K. Sugiyama, T. Sato, N. Itoh and N. Suzuki, *Ind. Eng. Chem. Res.*, 2016, **55**, 12742–12749.
9 D. A. Hansgen, D. G. Vlachos and J. G. Chen, *Nat. Chem.*, 2010, **2**, 484–489.
10 J. Li, W. Wang, W. Chen, Q. Gong, J. Luo, R. Lin, H. Xin, H. Zhang, D. Wang, Q. Peng, W. Zhu, C. Chen and Y. Li, *Nano Res.*, 2018, **11**, 4774–4785.
11 S. J. Wang, S. F. Yin, L. Li, B. Q. Xu, C. F. Ng and C. T. Au, *Appl. Catal., B*, 2004, **52**, 287–299.
12 A. M. Karim, V. Prasad, G. Mpourmpakis, W. W. Lonergan, A. I. Frenkel, J. G. Chen and D. G. Vlachos, *J. Am. Chem. Soc.*, 2009, **131**, 12230–12239.
13 Y. Li, L. Yao, Y. Song, S. Liu, J. Zhao, W. Ji and C. Au, *Chem. Commun.*, 2010, **46**, 5298.
14 D. Huang, C. Jiang, F. Liu, Y. Cheng, Y. Chen and K. Hsueh, *Int. J. Hydrogen Energy*, 2013, **38**, 3233–3240.
15 H. Zhang, Y. A. Alhamed, W. Chu, Z. Ye, A. AlZahrani and L. Petrov, *Appl. Catal., A*, 2013, **464**, 156–164.
16 Y. Li, J. Wen, A. M. Ali, M. Duan, W. Zhu, H. Zhang, C. Chen and Y. Li, *Chem. Commun.*, 2018, **54**, 6364–6367.
17 Y. Fujiwara, J. M. Lee, M. Tsujimoto, K. Kongpatpanich, T. Pila, K. Iimura, N. Tobori, S. Kitagawa and S. Horike, *Chem. Mater.*, 2018, **30**, 1830–1834.
18 J. S. J. Hargreaves, *Coord. Chem. Rev.*, 2013, **257**, 2015–2031.
19 Z. Schnepp, M. Thomas, S. Glatzel, K. Schlichte, R. Palkovits and C. Giordano, *J. Mater. Chem.*, 2011, **21**, 17760.
20 V. Tagliazucca, K. Schlichte, F. Schüth and C. Weidenthaler, *J. Catal.*, 2013, **305**, 277–289.
21 V. Tagliazucca, M. Leoni and C. Weidenthaler, *Phys. Chem. Chem. Phys.*, 2014, **16**, 6182–6188.
22 R. Pelka, K. Kiełbasa and W. Arabczyk, *J. Phys. Chem. C*, 2014, **118**, 6178–6185.
23 P. Yu, J. Guo, L. Liu, P. Wang, G. Wu, F. Chang and P. Chen, *ChemSusChem*, 2016, **9**, 364–369.
24 X. Duan, G. Qian, X. Zhou, D. Chen and W. Yuan, *Chem. Eng. J.*, 2012, **207–208**, 103–108.
25 J. Ji, X. Duan, G. Qian, X. Zhou, G. Tong and W. Yuan, *Int. J. Hydrogen Energy*, 2014, **39**, 12490–12498.
26 D. V. Leybo, A. N. Baiguzhina, D. S. Muratov, D. I. Arkhipov, E. A. Kolesnikov, V. V. Levina, N. I. Kosova and D. V. Kuznetsov, *Int. J. Hydrogen Energy*, 2016, **41**, 3854–3860.
27 S. F. Zaman, L. A. Jolaoso, S. Podila, A. A. Al-Zahrani, Y. A. Alhamed, H. Driss, M. M. Daous and L. Petrov, *Int. J. Hydrogen Energy*, 2018, **43**, 17252–17258.
28 L. A. Jolaoso, S. F. Zaman, S. Podila, H. Driss, A. A. Al-Zahrani, M. A. Daous and L. Petrov, *Int. J. Hydrogen Energy*, 2018, **43**, 4839–4844.

29 S. Podila, S. F. Zaman, H. Driss, A. A. Al-Zahrani, M. A. Daous and L. A. Petrov, *Int. J. Hydrogen Energy*, 2017, **42**, 8006–8020.

30 S. Podila, S. F. Zaman, H. Driss, Y. A. Alhamed, A. A. Al-Zahrani and L. A. Petrov, *Catal. Sci. Technol.*, 2016, **6**, 1496–1506.

31 S. Zaman, L. Jolaloso, A. Al-Zahrani, Y. Alhamed, S. Podila, H. Driss, M. Daous and L. Petrov, *Bulg. Chem. Commun.*, 2018, **50**, 181–188.

32 H. Zhang, Q. Gong, S. Ren, M. A. Arshid, W. Chu and C. Chen, *Catal. Sci. Technol.*, 2018, **8**, 907–915.

33 X. Fan, H. Zhang, J. Li, Z. Zhao, C. Xu, J. Liu, C. Xu and J. Liu, *Chin. J. Catal.*, 2014, **35**, 286–293.

34 S. Chouzier, P. Afanasiev, M. Vrinat, T. Cseri and M. Roy-Auberger, *J. Solid State Chem.*, 2006, **179**, 3314–3323.

35 X. Liu, J. Liu, Z. Chang, X. Sun and Y. Li, *Catal. Commun.*, 2011, **12**, 530–534.

36 J. Liu, S. Yang, W. Wu, Q. Tian, S. Cui, Z. Dai, F. Ren, X. Xiao and C. Jiang, *ACS Sustainable Chem. Eng.*, 2015, **3**, 2975–2984.

37 J. L. Rico and J. S. J. Hargreaves, *J. Mater. Sci.*, 2017, **52**, 5188–5193.

38 M. C. Biesinger, B. P. Payne, A. P. Grosvenor, L. W. M. Lau, A. R. Gerson and R. S. C. Smart, *Appl. Surf. Sci.*, 2011, **257**, 2717–2730.

39 D. M. Borsa and D. O. Boerma, *Hyperfine Interactions*, 2003, **151**, 31–48.

40 F. Yu, H. Zhou, Z. Zhu, J. Sun, R. He, J. Bao, S. Chen and Z. Ren, *ACS Catal.*, 2017, **7**, 2052–2057.

41 J. Yang, F. Zhang, X. Wang, D. He, G. Wu, Q. Yang, X. Hong, Y. Wu and Y. Li, *Angew. Chem., Int. Ed.*, 2016, **55**, 12854–12858.

42 S. F. Kurtoğlu and A. Uzun, *Sci. Rep.*, 2016, **6**, 32279.

43 J. Zhang, M. Comotti, F. Schueth, R. Schloegl and D. S. Su, *Chem. Commun.*, 2007, 1916–1918.

44 X. Duan, G. Qian, X. Zhou, Z. Sui, D. Chen and W. Yuan, *Appl. Catal., B*, 2011, **101**, 189–196.

45 A. Lu, J. Nitz, M. Comotti, C. Weidenthaler, K. Schlichte, C. W. Lehmann, O. Terasaki and F. Schüth, *J. Am. Chem. Soc.*, 2010, **132**, 14152–14162.

46 H. Z. Cui, Y. Q. Gu, X. X. He, S. Wei, Z. Jin, C. J. Jia and Q. S. Song, *Sci. Bull.*, 2016, **61**, 1–7.